

Emergence of topological nodal lines and type-II Weyl nodes in the strong spin-orbit coupling system InNbX_2 ($X=\text{S,Se}$)

Yongping Du,¹ Xiangyan Bo,² Di Wang,² Er-jun Kan,¹ Chun-Gang Duan,^{3,4} Sergey Y. Savrasov,^{5,*} and Xiangang Wan^{2,6,†}

¹*Department of Applied Physics, Nanjing University of Science and Technology, Nanjing, Jiangsu 210094, China*

²*National Laboratory of Solid State Microstructures and Department of Physics, Nanjing University, Nanjing 210093, China*

³*Key Laboratory of Polar Materials and Devices, Ministry of Education, East China Normal University, Shanghai 200241, China*

⁴*Collaborative Innovation Center of Extreme Optics, Shanxi University, Taiyuan, Shanxi 030006, China*

⁵*Department of Physics, University of California, Davis, One Shields Avenue, Davis, California 95616, USA*

⁶*Collaborative Innovation Center of Advanced Microstructures, Nanjing University, Nanjing 210093, China*

(Received 18 September 2017; published 29 December 2017)

Using first-principles density functional calculations, we systematically investigate electronic structures and topological properties of layered materials InNbX_2 ($X=\text{S, Se}$). In the absence of spin-orbit coupling (SOC), both compounds show nodal lines protected by mirror symmetry. Including SOC, the Dirac rings in InNbS_2 split into two Weyl rings. This unique property is distinguished from other discovered nodal-line materials, which normally require the absence of SOC. On the other hand, SOC breaks the nodal lines in InNbSe_2 , and the compound becomes a type-II Weyl semimetal with 12 Weyl points in the Brillouin zone. Using a supercell slab calculation, we study the dispersion of Fermi arc surface states in InNbSe_2 ; we also utilize a coherent potential approximation to probe their tolerance to the surface disorder effects. The quasi-two-dimensionality and the absence of toxic elements make these two compounds an ideal experimental platform for investigating novel properties of topological semimetals.

DOI: [10.1103/PhysRevB.96.235152](https://doi.org/10.1103/PhysRevB.96.235152)

I. INTRODUCTION

In the past few years, topological semimetals, such as Weyl semimetals (WSMs) [1,2], Dirac semimetals (DSMs) [3–9], and nodal-line semimetals (NLSs) [10–13], have received tremendous research interest. In a Weyl semimetal, the electrons around Weyl points, which are the crossing points of two nondegenerate linearly dispersing energy bands, behave exactly like Weyl fermions [1,2]. With definite chirality, each Weyl point can be considered a topologically protected charge, thus extending classification of topological phases of matter beyond insulators [1,2]. Weyl points are extremely robust against weak perturbations and can be annihilated only when pairs of Weyl points with opposite topological charge meet each other. Then the system opens a gap evolving into either a normal insulator or an axion insulator [1,14].

One of the most remarkable properties of WSMs is the existence of topological surface states in the form of Fermi arcs [1]. This serves as unambiguous evidence to identify this state of matter. A great number of other exotic phenomena have also been proposed for WSMs: a highly anisotropic negative magnetoresistance related to the chiral anomaly effect [15,16], a topological response [17], unusual nonlocal transport properties [18], novel quantum oscillations from Fermi arcs [19], etc.

A further classification here has been given to distinguish WSMs whose bulk Fermi surfaces shrink to Weyl points (called type I) and to exotic hyperboloid surfaces (called type II), where the cones are tilted and induce a finite density of states at the nodal point [20]. Due to the tilted nature of the nodes, the low-energy excitations break Lorentz invariance,

causing the absence of the chiral anomaly at certain magnetic-field angles, magnetic breakdown, and novel Klein tunneling [20,21].

There has been great progress in searching for signatures of WSMs in real materials. Starting from the original proposal on pyrochlore iridates [1], several systems, such as HgCr_2Se_4 [22], TaAs [23,24], WTe_2 [20], NbP [25], TaP [26], NbAs [27], MoTe_2 [28], MoP_2 , WP_2 [29], LaAlGe [30], etc., have been predicted to exhibit WSM behavior. A large amount of recent experimental work has been devoted to studying properties of the TaAs family [25–27,31–34]. In many of the proposed materials, however, the Weyl points do not exactly cross and are only close to the Fermi level, and also there are trivial Fermi states. The contribution from these trivial states significantly complicates the analysis of topological surface states and their novel transport behavior.

In addition to WSMs, a three-dimensional (3D) DSM [3–9] has also been proposed. The Dirac points in the DSM are fourfold degenerate and can be viewed as a merger of two Weyl fermions with opposite chirality in the Brillouin zone (BZ). The Dirac points usually require protection by time-reversal, inversion, and additional crystal symmetry [4–7].

Different from WSMs and DSMs, which have finite numbers of band-touching points in the BZ, a third topological semimetal, the NLS, has a whole crossing line in momentum space [10–13]. Just like the 3D DSM, the NLS also needs crystal symmetry to stabilize its band-crossing line [5,35]. The most exotic property of a NLS is its two-dimensional (2D) drumheadlike surface state [10–13,36–44]. It has been speculated that this special state may realize high-temperature superconductivity [45,46].

Several materials have been predicted to be topological NLSs [10–13,36–44]. However, most of these predictions are based on calculations without spin-orbit coupling (SOC) [11–13,36–42], the inclusion of which normally leads to gapping

*savrasov@physics.ucdavis.edu

†xgwan@nju.edu.cn

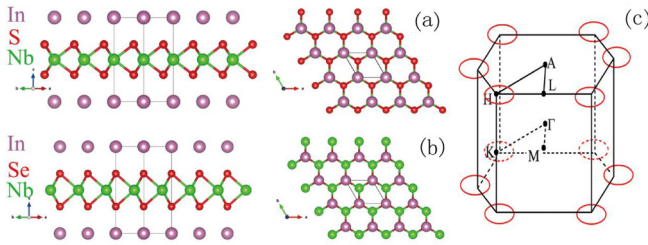


FIG. 1. (a) Side view (left) and top view (right) of the crystal structure of InNbS_2 . (b) Side view (left) and top view (right) of the crystal structure of InNbSe_2 . Green, violet, and red spheres represent Nb, In, and S (Se) atoms, respectively. (c) The schematic of the nodal lines in InNbX_2 ($X=\text{S,Se}$).

out the nodal line [11–13,36–42]. Only in a few systems was this found to not be the case, where TlTaSe_2 and PbTaSe_2 are predicted to retain NLS behavior in calculations with SOC [43,44].

Compared with 3D systems, quasi-2D layered materials are easier to cleave to study their surface electronic structures and are more favorable from the experimental perspective. Also, toxic elements like As, P, Tl, and Hg found in many of the discovered materials create additional complications. Thus, searching for new topological systems and finding ways to remove the effects of trivial states while preserving contributions from topological Fermi arcs are important problems of this emergent field of condensed-matter physics.

In this work, we use first-principles calculations based on density functional theory (DFT) in its generalized gradient approximation (GGA) [47] to predict that InNbS_2 and InNbSe_2 show nodal lines and Weyl semimetal behavior, respectively. Without considering SOC, both of them are NLSs, and the band-crossing lines are formed by fourfold-degenerate Dirac points. The nodal lines, which are located around the H point in the $k_z = \pi$ plane (i.e., the $L-H-A$ plane) in the BZ, are protected by the mirror symmetry. Including SOC, the fourfold-degenerate nodal line in InNbS_2 splits into two Weyl-type nodal lines which are again protected by the mirror symmetry. On the other hand, the SOC changes InNbSe_2 to a type-II WSM for which we predict the Fermi arc surface states to appear on an easily cleavable (001) indium-terminated surface. Using a combination of DFT with coherent potential approximation (CPA), we also simulate the effects of surface disorder to study the robustness of the Fermi arcs in this system. Our theoretical work shows that InNbS_2 and InNbSe_2 are very promising materials for studying NLSs and WSMs, respectively.

II. CRYSTAL STRUCTURE

InNbX_2 compounds ($X=\text{S, Se}$) have already been synthesized experimentally, and their crystal structures belong to space group $P\bar{6}m2$ (No. 187), which is noncentrosymmetric [48–50]. The In layer is intercalated between two niobium dichalcogenides layers. As shown in Figs. 1(a) and 1(b), the mirror plane is located in the In layer or Nb layer. As discussed later, this mirror plane plays a key role in protecting the nodal line. As shown in Fig. 1, the In atoms in InNbS_2 are aligned with Nb atoms in the vertical direction, while in

InNbSe_2 , they are aligned with Se atoms. This difference in the lattice structure results in different topological features for these two compounds. We also fully relax the lattice constants and the coordinates of atoms included in van der Waals interaction [51]. The numerical results are in good agreement with experiments [52], and the small discrepancy between the numerical and experimental structures has a negligible effect on the electronic property. Hence, the following results are obtained based on the experimental structure, unless specifically stated otherwise.

III. RESULTS FOR InNbS_2

Here we discuss our band structure results for InNbS_2 . We perform the density functional GGA calculation by using a full-potential linear muffin-tin orbital (FP-LMTO) method [53] and also cross-check the results with the linearized augmented plane-wave method as implemented in the WIEN2K package [54]. Both methods provide identical electronic structures. The orbital character analysis shows that $3s$ and $3p$ bands of S atoms are mainly located at -14 to -12 and -7 to -1 eV, respectively. This indicates that the S $3s$ and S $3p$ orbits are almost completely filled. The Nd $5d$ states, which are mainly located between -1 and 4 eV, also have a spectral weight between -7 and -1 eV, indicating a considerable hybridization between Nb and S. On the other hand, In $5p$ bands are distributed mainly above -1 eV. As shown in Fig. 2(a), the bands around the Fermi level are mainly contributed by Nb $5d_{x^2-y^2}/5d_{xy}$ and In $6p_x/6p_y$ states. The Nb $5d_{x^2-y^2}/5d_{xy}$ bands are higher in energy than the In $6p_x/6p_y$ states; however, there is a band inversion around the H point, as shown in Fig. 2(c). This band inversion has also been confirmed by the modified Becke-Johnson (mBJ) exchange potential calculations [55]. Since the $L-H-A$ plane possesses mirror symmetry, the In $6p_x/6p_y$ (Nb $5d_{x^2-y^2}/5d_{xy}$) states around the H point can be classified in terms of the mirror eigenvalue -1 ($+1$), as shown in Fig. 2(c). Combined with the time-reversal symmetry, this band inversion guarantees a nodal line in the $L-H-A$ plane [43,44]. The schematic of the nodal lines in InNbS_2 is shown in Fig. 1(c).

To clarify the origin of the band inversion at the H point, we calculate the electronic structure of InNbS_2 by applying an in-plane tensile strain. We denote the magnitude of the in-plane strain by $(a - a_0)/a_0$, where a and a_0 denote lattice parameters of the strained and unstrained systems, respectively. Our calculation reveals that the energy difference between In $6p_x/6p_y$ states and Nb $5d_{x^2-y^2}/5d_{xy}$ states decreases as the in-plane tensile strain increases, and when the in-plane strain becomes larger than 7%, the band inversion at the H point disappears. Therefore, the band inversion originates from the crystal-field effect instead of SOC.

To explore the role of the mirror symmetry, we break it by shifting a Nb atom by 0.01 \AA along the z direction. Without mirror symmetry, the In $6p_x/6p_y$ and Nb $5d_{x^2-y^2}/5d_{xy}$ states belong to the same irreducible representation and can hybridize with each other. Thus, the band crossing around the H point becomes gapped, as shown in Fig. 2(e). This clearly demonstrates that the nodal line in InNbS_2 is indeed protected by the mirror symmetry.

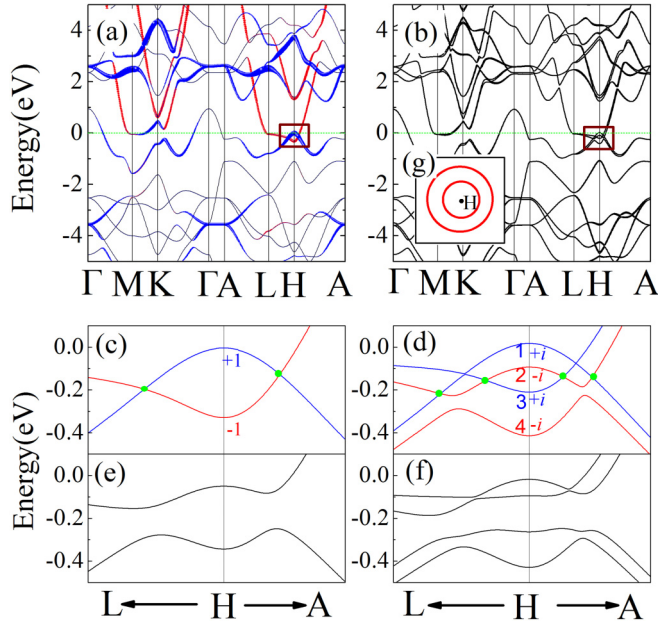


FIG. 2. (a) Calculated bulk band structure of InNbS₂ without SOC. The weights of In $6p_x/6p_y$ (Nb $5d_{x^2-y^2}/5d_{xy}$) states are proportional to the width of the red (blue) curves. (b) Bulk band structure of InNbS₂ calculated with the inclusion of SOC. (c) Close-up of the band structure around the H point as marked in (a). The red line denotes the In $6p_x/6p_y$ states which belong to the irreducible representation Γ_2 of the space group, while the blue one is the state of Nb $5d_{x^2-y^2}/5d_{xy}$ belonging to the irreducible representation Γ_1 of the space group. The red band has a mirror eigenvalue of -1 , while the blue one has a mirror eigenvalue of $+1$. (d) Close-up of the band structure around the H point near the Fermi energy as marked in (b). Red denotes the mirror eigenvalue $-i$, while green denotes the mirror eigenvalue i . (e) and (f) Band structures around the H point with the mirror symmetry broken by shifting the Nb atom slightly away from the equilibrium position without and with SOC, respectively. (g) The schematic of the nodal lines around the H point in InNbS₂ when including SOC.

As a relativistic effect, SOC always exists. Thus, we also perform the calculation to check the effect of SOC. Without inversion, SOC splits each band into two branches, as shown in Fig. 2(b). As a result, there are spinful bands near the Fermi level, as shown in Fig. 2(d). Due to the mirror symmetry in the $L-H-A$ plane, we can classify these four bands by mirror eigenvalues of $\pm i$. The two red bands have mirror eigenvalues of $-i$, while the blue ones have mirror eigenvalues of i . As a result, the order of mirror eigenvalues of the four bands is $(+i, -i, +i, -i)$ (sorting from high energy to low energy at the H point, labeled as bands 1, 2, 3, 4), as shown in Fig. 2(d). Since SOC does not eliminate the band inversion, two bands with different mirror eigenvalues form two separate Weyl rings around the H point. Furthermore, the nodal line can be characterized by the Berry phase [10–13,36–44]; our numerical results show that the Berry phases of these two separate Weyl rings are the same, i.e., π . These two unique separated nodal lines can have unique surface states, as discussed in Refs. [42–44]. When mirror symmetry is broken, the four bands around the H point are found to belong to the same irreducible representation. Consequently, the Weyl rings

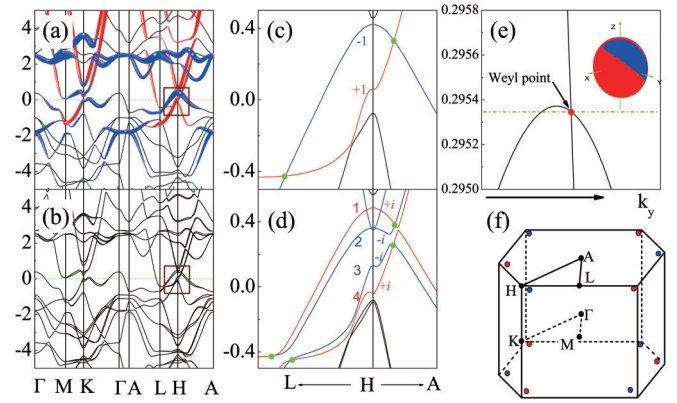


FIG. 3. (a) Bulk band structure of InNbSe₂ without SOC. The weights of In $6p_x/6p_y$ (Nb $5d_{x^2-y^2}/5d_{xy}$) states are proportional to the width of the red (blue) curves. (b) Bulk band structure of InNbSe₂ including SOC. (c) Close-up of the band structure around the H point as marked in (a). The red curve denotes a mirror eigenvalue of $+1$, while the blue curve denotes a mirror eigenvalue of -1 . (d) Close-up of the band structure around the H point as marked in (b). The red curve denotes a mirror eigenvalue of $+i$, and the blue curve denotes a mirror eigenvalue of $-i$. (e) Band structure around the Weyl point. The direction is parallel to the k_y axis and crosses the Weyl point. The inset is the value of $|T(k)|/|U(k)|$; the magnetic field within the blue area [i.e., $|T(k)|/|U(k)| > 1$] can induce negative magnetoresistance, while the red one [$|T(k)|/|U(k)| < 1$] cannot have negative magnetoresistance [20]. (f) The schematic of the Weyl points in the first Brillouin zone. Blue (red) denotes a Chern number of $+1$ (-1).

are gapped out as shown in Fig. 2(f). This again shows that the mirror symmetry plays a key role in protecting the nodal lines in InNbS₂.

IV. RESULTS FOR InNbSe₂

We now discuss our band structure calculation for InNbSe₂. The results without and with SOC are shown in Figs. 3(a) and 3(b), respectively. Our orbital-character analysis reveals that the states near the Fermi level are mainly contributed by Nb $5d_{x^2-y^2}/5d_{xy}$ (denoted by red) and In $6p_x/6p_y$ (denoted by blue). However, both GGA and mBJ calculations predict that the energy of Nb $5d_{x^2-y^2}/5d_{xy}$ is higher than In $6p_x/6p_y$ at the H point. As a result, there is also a band inversion around the H point, like in the case of InNbS₂. This is shown in Fig. 3(a). Again, based on the mirror symmetry, the bands around the H point can be classified by their mirror eigenvalues. In Fig. 3(c), the band with a mirror eigenvalue of -1 ($+1$) is marked in blue (red). Thus, like for InNbS₂, time-reversal symmetry and the band inversion result in a nodal line around the H point at the mirror plane.

When SOC is included in the calculation, two crossing bands around the H point split into four bands, as shown in Fig. 3(b). The detailed band structure around the H point marked in Fig. 3(b) is shown in Fig. 3(d). Different from the situation for InNbS₂, the order of the mirror eigenvalues at the H point of the four bands near the Fermi energy is $(+i, -i, -i, +i)$ (sorting from high energy to low energy and labeled as bands 1, 2, 3, 4). Thus, two bands with the same eigenvalues

(i.e., bands 2 and 3 with eigenvalues of $-i$) are hybridized and open a gap, other than Weyl rings. However, further analysis shows that there are band crossing points between bands 1 and 2 and bands 3 and 4. The mirror eigenvalues between them are different; thus, band crossings between them form two Weyl rings protected by mirror symmetry on the $L-H-A$ plane. The different orders of mirror eigenvalues and band structures between InNbS_2 and InNbSe_2 are caused by the different positions of In atoms. To further confirm this, we calculate the electronic structure of InNbSe_2 in the structure of InNbS_2 and vice versa. Our calculations show that, when InNbSe_2 is in the structure of InNbS_2 , it becomes a node-line semimetal with two separate Weyl rings around the H point exactly like the case for InNbS_2 . And when InNbS_2 is in

$$\gamma_{P_l,s}^n = \text{Im} \ln[\langle n(\mathbf{k}_l,s) | n(\mathbf{k}_l + \mathbf{u}_1,s) \rangle \langle n(\mathbf{k}_l + \mathbf{u}_1,s) | n(\mathbf{k}_l + \mathbf{u}_1 + \mathbf{u}_2,s) \rangle \langle n(\mathbf{k}_l + \mathbf{u}_1 + \mathbf{u}_2,s) | n(\mathbf{k}_l + \mathbf{u}_2,s) \rangle \langle n(\mathbf{k}_l + \mathbf{u}_2,s) | n(\mathbf{k}_l,s) \rangle],$$

where \mathbf{k}_l is a vector at the l th mesh point, $s = 1-6$ denotes each of the six faces of the cube, \mathbf{u}_1 and \mathbf{u}_2 are vectors between the nearest mesh points for the two directions of the \mathbf{k} vector on the surface of the cube, and P_l is l th smallest closed path passing by the point \mathbf{k}_l and its nearest mesh points. In this formula, the Chern number is given by the sum over the coarse mesh of phases $\gamma_{P_l,s}^n$: $C_n = \sum_{P_l,s} \gamma_{P_l,s}^n$. The Bloch wave functions $|n(\mathbf{k}_l,s)\rangle$ are obtained from our first-principles calculations. We employ the 15×15 k mesh on each of the six faces of the cube, which we found to be sufficient for numerical convergence. We calculate the Chern number of the Weyl point located at (0.298, 0.298, 0.444) using this method and obtain a numerical result equal to $+1$. The location of this and other Weyl points is schematically shown in Fig. 3(f).

We notice that the Weyl points here exist at the boundaries between electron and hole pockets; therefore, the compound can be classified as a type-II WSM. Figure 3(e), which shows a detailed band dispersion in the vicinity of one Weyl point, is very similar to the case of WTe_2 [20], where this new type of Weyl point was recently introduced. The type-II WSM appear due to the tilting term in the linear Weyl Hamiltonian which has led to a finer classification of topological semimetals [20]. Around the Weyl points, the energy spectrum can be written as $\epsilon_{\pm}(k) = T(k) \pm U(k)$. As a result, we expect that InNbSe_2 will display negative magnetoresistance related to the chiral anomaly only when the direction of the magnetic field falls within the cone where $|T(k)|/|U(k)| > 1$ [20] [i.e., the blue area in Fig. 3(e)]. We monitor the contact between electron and hole pockets in InNbSe_2 by computing the constant-energy surface with a slightly shifted position (up by 0.2 eV) of the Fermi level for a stoichiometric compound. The result is shown in Fig. 4(a), where the green-magenta surface is the hole pocket, while the red-blue one is the electron pocket. We can see that the hole pocket almost touches the electron pocket near the position of the Weyl point. Figure 4(b) shows the same information in the immediate vicinity of the Weyl point together with the spin distribution of electronic states, shown by arrows. For an ideal Weyl Hamiltonian, the spins are either parallel or antiparallel to the velocities corresponding to the positive or negative chiralities. In real compounds such

the same structure as InNbSe_2 , the bands are hybridized and open a gap instead of forming two crossing lines. Interestingly, our further calculation shows that InNbSe_2 becomes a Weyl semimetal with 12 Weyl nodes in the first BZ, as shown in Figs. 3(e) and 3(f). These 12 Weyl points are related to each other by crystal symmetry; consequently, they have the same energy. The Weyl points are searched for by scanning the whole BZ.

To confirm the existence of the Weyl points in InNbSe_2 , we perform Berry curvature integration based on a computational scheme proposed by Fukui *et al.* [56]. We define a small cubic region surrounding each Weyl point. The quantity $\gamma_{P_l,s}^n$, which is often called the field strength, is defined as [56,57]

as InNbSe_2 , which is considered here, this becomes only approximate, and as seen in Fig. 4(b), spins show a rather high degree of anisotropy.

V. FERMI ARCS AND THE EFFECT OF SURFACE DISORDER

In order to examine the Fermi arc surface states of InNbSe_2 we determine the one-electron energy bands of a 6-unit-cell (24 atomic layers) slab structure using the FP-LMTO method [53]. The slab is extended along the (001) direction and terminated by a Se atomic layer on the top and by an In atomic layer on the bottom. The spacing between the slabs is set to 12 Å. The distance between In and Se atoms is largest in the original unit cell, which together with the quasi-two-dimensionality of the crystal structure indicates that this should be the most easily cleavable surface in an experimental setup.

In order to compute the surface Fermi states, we compute surface-projected imaginary Green's functions:

$$\text{Im}G(\mathbf{k}, E) = \text{Im} \sum_j \frac{\langle \mathbf{k}_j | \hat{P}_s | \mathbf{k}_j \rangle}{E - E_{\mathbf{k}_j} - i\delta},$$

where we set $\delta = 0.001$ Ry and the surface-projector operator \hat{P}_s is chosen as a sum over four top and bottom atomic

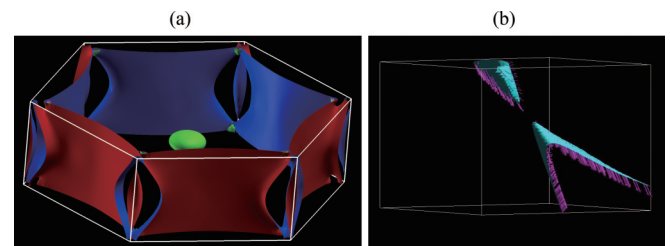


FIG. 4. Calculated constant-energy surface with a slightly shifted position (up by 0.2 eV) of the Fermi level for stoichiometric InNbSe_2 showing type-II character of the predicted Weyl semimetal: (a) the green-magenta surface is the hole pocket, while the red-blue one is the electron pocket. (b) The same but in the immediate vicinity of the Weyl point. Arrows show spin directions of the one-electron states.

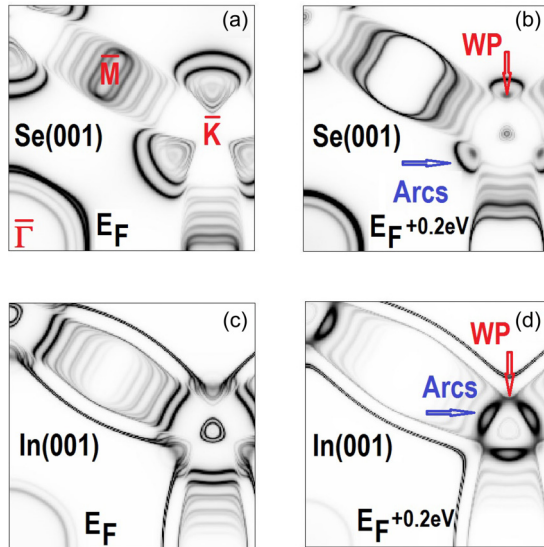


FIG. 5. Surface Fermi states of the InNbSe₂ slab for the (a) and (b) Se-terminated and (c) and (d) In-terminated (001) surfaces. The position of the Fermi level in (a) and (c) corresponds to the stoichiometric compound. (b) and (d) show Fermi surfaces corresponding to the Fermi level shifted by 0.2 eV when it is tuned to the Weyl points to better visualize the appearance of the Fermi arcs.

layers τ ,

$$\hat{P}_s = \sum_{lm\tau} |\phi_{lm\tau}\rangle \langle \phi_{lm\tau}|.$$

Here $\phi_{lm\tau}$ are the solutions of the radial Schrodinger equation inside a muffin-tin sphere of atom τ taken with the spherically symmetric part of the potential [58].

Figure 5 shows the result of our calculation, where we visualize $\text{Im}G(\mathbf{k}, E)$ as a function of \mathbf{k} by a color (white is 0, and black is $1/\delta = 1000$) within a part of the planar BZ corresponding to the (001) surface unit cell. We distinguish cases for Se-terminated [Figs. 5(a) and 5(b)] and In-terminated [Figs. 5(c) and 5(d)] surfaces. Since the Weyl points are located not exactly at the Fermi level, we plot $\text{Im}G(\mathbf{k}, E)$ for the energy $E = E_F$ [Figs. 5(a) and 5(c)], as well as for the energy $E = E_F + 0.2$ eV [Figs. 5(b) and 5(d)], which corresponds to the location of the Weyl points. We note that although the (001) surface should be easy to cleave, the chosen atomic configuration assumes that the Weyl points of opposite chiralities project onto the same \mathbf{k} point in the surface BZ. This means that the Fermi arcs extending between opposite chiral charges can potentially start and end at the same projected Weyl point. We found this to be the case for the Se-terminated surface, where small arcs are clearly visible, especially in Fig. 5(b), which corresponds to the position of the Fermi level tuned to the Weyl point. The situation is more complicated for the In-terminated surface where there are essentially two lines that are resolved as connecting the Weyl points on Fig. 5(d). We interpret one line to be potentially the Fermi arc and the other one to be either a regular surface state or a bulk Fermi state projected to the surface BZ.

In a recent work [59] we argued, based on a simulation of a tight-binding model, that the Fermi arcs should be more surface

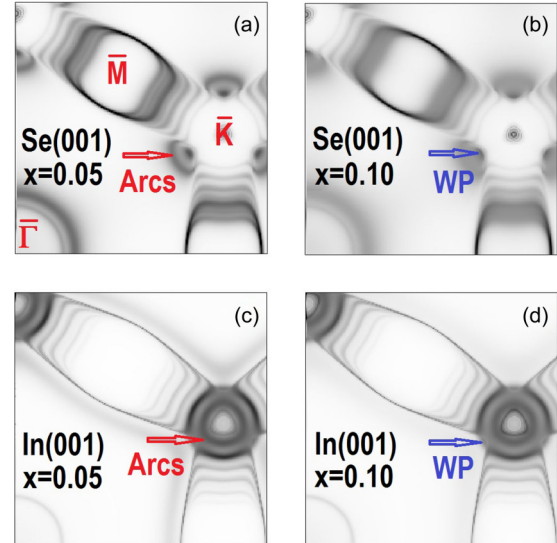


FIG. 6. Effect of surface vacancies on the surface Fermi states of the InNbSe₂ slab for the (a) and (b) Se-terminated and (c) and (d) In-terminated (001) surfaces. (a) and (c) correspond to 5% of vacancies imposed at the top Se and bottom In layers, respectively. (b) and (d) correspond to 10% of the vacancies. The Fermi level is tuned to the position of the Weyl points to better illustrate the degradation of the Fermi arc states.

disorder tolerant than the regular surface states, especially in the vicinity of the Weyl points where the arcs' electronic wave functions are extended well into the bulk and become less sensitive to the surface disorder. We also found that the particular sensitivity to the surface disorder depends on the shape of the Fermi arc, with the straight arc geometry showing the most disorder tolerance. Surface disorder is inevitable in a real experimental setting, with vacancies being its primary source. It is therefore interesting to examine this effect in our proposed InNbSe₂ WSM.

In order to perform a simulation of vacancies on the surface of InNbSe₂, we use a combination of DFT with a CPA [60], a self-consistent method that allows us to extract disorder-induced self-energies $\hat{\Sigma}_{CPA}(E)$ from the FP-LMTO calculation. Our recent implementation within the FP-LMTO method is described in Ref. [59]. Figures 6(a) and 6(b) show the evolution of the one-electron Fermi states of the InNbSe₂ slab structure that are projected onto the Se-terminated surface for two concentrations, $x = 0.05$ and $x = 0.1$, of substitutional vacancies that we impose on the topmost Se layer. For both concentrations, the Fermi arcs are still visible, and increasing the disorder results in broadening the arcs, especially in the regions always from the Weyl points. Since the arcs' electrons are continuously connected to the bulk Weyl points, the area in the vicinity of the Weyl points is less affected by disorder. We can contrast this behavior with the regular surface states, which we expect to be more susceptible to surface disorder. We do not impose any bulk disorder in this calculation; therefore, the bulk states projected onto the surface BZ are unaffected by the surface vacancies.

The situation is more complicated for the Fermi arcs appearing on the In-terminated (001) surface. Figures 6(c) and 6(d) show their behavior for $x = 0.05$ and $x = 0.1$,

respectively. We notice that the arcs that connect the Weyl points in Fig. 5(d) slightly change their shape with disorder, which is possibly connected to the effect induced by the real part of the disorder self-energy $\text{Re}\Sigma_{CPA}(E = E_F)$. One state is seen in this simulation to get closer to the \bar{K} point of the surface BZ, while another state has a shape resembling a regular bulk Fermi state projected onto the surface BZ. Both states acquire much less broadening if we compare them with other surface states that broaden a lot and almost disappear when $x = 0.1$. As these arcs show a lot less curvature than the arcs resolved on the Se-terminated surface, we therefore speculate that this is likely the effect of the disorder tolerance for the straight Fermi arcs that we proposed in our recent work [59].

VI. SUMMARY

In summary, by using first-principles calculations, we investigated the topological properties of the layered materials InNbS_2 and InNbSe_2 . Our theoretical analysis showed that InNbS_2 is a nodal-line semimetal even with the presence of SOC as long as the mirror symmetry is preserved. This signif-

icant feature is different from previously proposed materials which normally neglect the SOC. InNbSe_2 is proposed to be a type-II WSM with 12 Weyl nodes at the same energy level. We also studied the Fermi arc surface states and confirmed their robustness against the surface disorder effects. These two compounds are quasi-2D and easy to cleave; therefore, they can potentially serve as an interesting platform for further experimental studies of topological electronic states.

ACKNOWLEDGMENTS

This work was supported by the National Key Research and Development Program of China (Grant No. 2017YFA0303203), the National Natural Science Foundation of China (Grants No. 11525417, No. 11790311, No. 51572085, No. 51721001), the National Key Project for Basic Research of China (Grant No. 2014CB921104), the Natural Science Foundation of Jiangsu Province (Grant No. BK20170821), and the Priority Academic Program Development of Jiangsu Higher Education Institutions. S.Y.S. was supported by NSF DMR (Grant No. 1411336).

-
- [1] X. Wan, A. M. Turner, A. Vishwanath, and S. Y. Savrasov, Topological semimetal and Fermi-arc surface states in the electronic structure of pyrochlore iridates, *Phys. Rev. B* **83**, 205101 (2011).
- [2] L. Balents, Viewpoint: Weyl electrons kiss, *Physics* **4**, 36 (2011).
- [3] S. M. Young, S. Zaheer, J. C. Y. Teo, C. L. Kane, E. J. Mele, and A. M. Rappe, Dirac Semimetal in Three Dimensions, *Phys. Rev. Lett.* **108**, 140405 (2012).
- [4] B.-J. Yang, and N. Nagaosa, Classification of stable three-dimensional Dirac semimetals with nontrivial topology, *Nat. Commun.* **5**, 4898 (2014); Z. Gao, M. Hua, H. Zhang, and X. Zhang, Classification of stable Dirac and Weyl semimetals with reflection and rotational symmetry, *Phys. Rev. B* **93**, 205109 (2016).
- [5] X.-L. Sheng, Z. Wang, R. Yu, H. Weng, Z. Fang, and X. Dai, Topological insulator to Dirac semimetal transition driven by sign change of spin-orbit coupling in thallium nitride, *Phys. Rev. B* **90**, 245308 (2014).
- [6] Z. Wang, Y. Sun, X.-Q. Chen, C. Franchini, G. Xu, H. Weng, X. Dai, and Z. Fang, Dirac semimetal and topological phase transitions in $A_3\text{Bi}$ ($A = \text{Na}, \text{K}, \text{Rb}$), *Phys. Rev. B* **85**, 195320 (2012).
- [7] Z. Wang, H. M. Weng, Q. Wu, X. Dai, and Z. Fang, Three-dimensional Dirac semimetal and quantum transport in Cd_3As_2 , *Phys. Rev. B* **88**, 125427 (2013).
- [8] Q. D. Gibson, L. M. Schoop, L. Muechler, L. S. Xie, M. Hirschberger, N. P. Ong, R. Car, and R. J. Cava, Three-dimensional Dirac semimetals: Design principles and predictions of new materials, *Phys. Rev. B* **91**, 205128 (2015).
- [9] Y. Du, B. Wan, D. Wang, L. Sheng, C.-G. Duan, and X. Wan, Dirac and Weyl Semimetal in XYBi ($X = \text{Ba}, \text{Eu}$; $Y = \text{Cu}, \text{Ag}$ and Au), *Sci. Rep.* **5**, 14423 (2015).
- [10] A. A. Burkov, M. D. Hook, and L. Balents, Topological nodal semimetals, *Phys. Rev. B* **84**, 235126 (2011).
- [11] H. Weng, Y. Liang, Q. Xu, R. Yu, Z. Fang, X. Dai, and Y. Kawazoe, Topological node-line semimetal in three-dimensional graphene networks, *Phys. Rev. B* **92**, 045108 (2015).
- [12] R. Yu, H. Weng, Z. Fang, X. Dai, and X. Hu, Topological Node-Line Semimetal and Dirac Semimetal State in Antiperovskite Cu_3PdN , *Phys. Rev. Lett.* **115**, 036807 (2015).
- [13] Y. Kim, B. J. Wieder, C. L. Kane, and A. M. Rappe, Dirac Line Nodes in Inversion-Symmetric Crystals, *Phys. Rev. Lett.* **115**, 036806 (2015).
- [14] X. Wan, A. Vishwanath, and S. Y. Savrasov, Computational Design of Axion Insulators Based on $5d$ Spinel Compounds, *Phys. Rev. Lett.* **108**, 146601 (2012).
- [15] V. Aji, Adler-Bell-Jackiw anomaly in Weyl semimetals: Application to pyrochlore iridates, *Phys. Rev. B* **85**, 241101 (2012).
- [16] D. T. Son and B. Z. Spivak, Chiral anomaly and classical negative magnetoresistance of Weyl metals, *Phys. Rev. B* **88**, 104412 (2013).
- [17] K.-Y. Yang, Y.-M. Lu, and Y. Ran, Quantum Hall effects in a Weyl semimetal: Possible application in pyrochlore iridates, *Phys. Rev. B* **84**, 075129 (2011).
- [18] S. A. Parameswaran, T. Grover, D. A. Abanin, D. A. Pesin, and A. Vishwanath, Probing the Chiral Anomaly with Nonlocal Transport in Three-Dimensional Topological Semimetals, *Phys. Rev. X* **4**, 031035 (2014).
- [19] A. C. Potter, I. Kimchi, and A. Vishwanath, Quantum oscillations from surface Fermi arcs in Weyl and Dirac semimetals, *Nat. Commun.* **5**, 5161 (2014).
- [20] A. A. Soluyanov, D. Gresch, Z. Wang, Q. Wu, M. Troyer, X. Dai, and B. A. Bernevig, Type-II Weyl semimetals, *Nature (London)* **527**, 495 (2015).
- [21] T. E. O'Brien, M. Diez, and C. W. J. Beenakker, Magnetic Breakdown and Klein Tunneling in a Type-II Weyl Semimetal, *Phys. Rev. Lett.* **116**, 236401 (2016).
- [22] G. Xu, H. M. Weng, Z. Wang, X. Dai, and Z. Fang, Chern Semimetal and the Quantized Anomalous Hall Effect in HgCr_2Se_4 , *Phys. Rev. Lett.* **107**, 186806 (2011).

- [23] H. Weng, C. Fang, Z. Fang, B. A. Bernevig, and X. Dai, Weyl Semimetal Phase in Noncentrosymmetric Transition-Metal Monophosphides, *Phys. Rev. X* **5**, 011029 (2015).
- [24] S.-M. Huang, S.-Y. Xu, I. Belopolski, C.-C. Lee, G. Chang, B. Wang, N. Alidoust, G. Bian, M. Neupane, C. Zhang, S. Jia, A. Bansil, H. Lin, and M. Z. Hasan, A Weyl Fermion semimetal with surface Fermi arcs in the transition metal monpnictide TaAs class, *Nat. Commun.* **6**, 7373 (2015).
- [25] C. Shekhar, A. K. Nayak, Y. Sun, M. Schmidt, M. Nicklas, I. Leermakers, U. Zeitler, Y. Skourski, J. Wosnitzer, Z. Liu, Y. Chen, W. Schnelle, H. Borrmann, Y. Grin, C. Felser, and B. Yan, Extremely large magnetoresistance and ultrahigh mobility in the topological Weyl semimetal candidate NbP, *Nat. Phys.* **11**, 645 (2015).
- [26] N. Xu, H. M. Weng, B. Q. Lv, C. E. Matt, J. Park, F. Bisti, V. N. Strocov, D. Gawryluk, E. Pomjakushina, K. Conder, N. C. Plumb, M. Radovic, G. Autès, O. V. Yazyev, Z. Fang, X. Dai, T. Qian, J. Mesot, H. Ding, and M. Shi, Observation of Weyl nodes and Fermi arcs in tantalum phosphide, *Nat. Commun.* **7**, 11006 (2016).
- [27] S. Xu, N. Alidoust, I. Belopolski, Z. Yuan, G. Bian, T.-R. Chang, H. Zheng, V. N. Strocov, D. S. Sanchez, G. Chang, C. Zhang, D. Mou, Y. Wu, L. Huang, C.-C. Lee, S.-M. Huang, B. Wang, A. Bansil, H.-T. Jeng, T. Neupert, A. Kaminski, H. Lin, S. Jia, and M. Z. Hasan, Discovery of a Weyl fermion state with Fermi arcs in niobium arsenide, *Nat. Phys.* **11**, 748 (2015).
- [28] L. Huang, T. M. McCormick, M. Ochi, Z. Zhao, M.-T. Suzuki, R. Arita, Y. Wu, D. Mou, H. Cao, J. Yan, N. Trivedi, and A. Kaminski, Spectroscopic evidence for a type II Weyl semimetallic state in MoTe₂, *Nat. Mater.* **15**, 1155 (2016).
- [29] G. Autès, D. Gresch, M. Troyer, A. A. Soluyanov, and O. V. Yazyev, Robust Type-II Weyl Semimetal Phase in Transition Metal Diphosphides XP₂ (X = Mo, W), *Phys. Rev. Lett.* **117**, 066402 (2016).
- [30] S.-Y. Xu, N. Alidoust, G. Chang, H. Lu, B. Singh, I. Belopolski, D. S. Sanchez, X. Zhang, G. Bian, H. Zheng, M.-A. Hsuanu, Y. Bian, S.-M. Huang, C.-H. Hsu, T.-R. Chang, H.-T. Jeng, A. Bansil, T. Neupert, V. N. Strocov, H. Lin, S. Jia, and M. Z. Hasan, Discovery of Lorentz-violating type II Weyl fermions in LaAlGe, *Sci. Adv.* **3**, e1603266 (2017).
- [31] B. Q. Lv, H. M. Weng, B. B. Fu, X. P. Wang, H. Miao, J. Ma, P. Richard, X. C. Huang, L. X. Zhao, G. F. Chen, Z. Fang, X. Dai, T. Qian, and H. Ding, Experimental Discovery of Weyl Semimetal TaAs, *Phys. Rev. X* **5**, 031013 (2015).
- [32] B. Q. Lv, N. Xu, H. M. Weng, J. Z. Ma, P. Richard, X. C. Huang, L. X. Zhao, G. F. Chen, C. E. Matt, F. Bisti, V. N. Strocov, J. Mesot, Z. Fang, X. Dai, T. Qian, M. Shi, and H. Ding, Observation of Weyl nodes in TaAs, *Nat. Phys.* **11**, 724 (2015).
- [33] S.-Y. Xu, I. Belopolski, N. Alidoust, M. Neupane, G. Bian, C. Zhang, R. Sankar, G. Chang, Z. Yuan, C.-C. Lee, S.-M. Huang, H. Zheng, J. Ma, D. S. Sanchez, B. Wang, A. Bansil, F. Chou, P. P. Shibayev, H. Lin, S. Jia, M. Z. Hasan, Discovery of a Weyl fermion semimetal and topological Fermi arcs, *Science* **349**, 613 (2015).
- [34] D.-F. Xu, Y. Du, Z. Wang, Y.-P. Li, X.-H. Niu, Q. Yao, P. Dudin, Z.-A. Xu, X. Wan, D.-L. Feng, Observation of Fermi Arcs in Non-centrosymmetric Weyl Semi-Metal Candidate NbP, *Chin. Phys. Lett.* **32**, 107101 (2015).
- [35] C. Fang, Y. Chen, H.-Y. Kee, and L. Fu, Topological nodal line semimetals with and without spin-orbital coupling, *Phys. Rev. B* **92**, 081201 (2015).
- [36] Q. Xu, R. Yu, Z. Fang, X. Dai, and H. Weng, Topological nodal line semimetals in the CaP₃, *Phys. Rev. B* **95**, 045136 (2017).
- [37] H. Huang, J. Liu, D. Vanderbilt, and W. Duan, Topological nodal-line semimetals in alkaline-earth stannides, germanides, and silicides, *Phys. Rev. B* **93**, 201114 (2016).
- [38] Y. Du, F. Tang, D. Wang, L. Sheng, E.-j. Kan, C.-G. Duan, S. Y. Savrasov, and X. Wan, CaTe: A new topological node-line and Dirac semimetal, *npj Quantum Mater.* **2**, 3 (2017).
- [39] K. Mullen, B. Uchoa, and D. T. Glatzhofer, Line of Dirac Nodes in Hyperhoneycomb Lattices, *Phys. Rev. Lett.* **115**, 026403 (2015).
- [40] L. Xie, L. M. Schoop, E. M. Seibel, Q. D. Gibson, W. Xie, and R. J. Cava, A new form of Ca₃P₂ with a ring of Dirac nodes, *APL Mater.* **3**, 083602 (2015).
- [41] M. Zeng, C. Fang, G. Chang, Y.-A. Chen, T. Hsieh, A. Bansil, H. Lin, and L. Fu, Topological semimetals and topological insulators in rare earth monpnictides, [arXiv:1504.03492](https://arxiv.org/abs/1504.03492).
- [42] Y.-H. Chan, C.-K. Chiu, M. Y. Chou, and A. P. Schnyder, Ca₃P₂ and other topological semimetals with line nodes and drumhead surface states, *Phys. Rev. B* **93**, 205132 (2016).
- [43] G. Bian, T.-R. Chang, H. Zheng, S. Velury, S.-Y. Xu, T. Neupert, C.-K. Chiu, S.-M. Huang, D. S. Sanchez, I. Belopolski, N. Alidoust, P.-J. Chen, G. Chang, A. Bansil, H.-T. Jeng, H. Lin, and M. Z. Hasan, Drumhead surface states and topological nodal-line fermions in TlTaSe₂, *Phys. Rev. B* **93**, 121113(R) (2016).
- [44] G. Bian, T.-R. Chang, R. Sankar, S.-Y. Xu, H. Zheng, T. Neupert, C.-K. Chiu, S.-M. Huang, G. Chang, I. Belopolski, D. S. Sanchez, M. Neupane, N. Alidoust, C. Liu, B. Wang, C.-C. Lee, H.-T. Jeng, C. Zhang, Z. Yuan, S. Jia, A. Bansil, F. Chou, H. Lin, and M. Z. Hasan, Topological nodal-line fermions in spin-orbit metal PbTaSe₂, *Nat. Commun.* **7**, 10556 (2015).
- [45] T. T. Heikkilä and G. E. Volovik, Flat bands as a route to high-temperature superconductivity in graphite, [arXiv:1504.05824](https://arxiv.org/abs/1504.05824).
- [46] N. B. Kopnin, T. T. Heikkilä, and G. E. Volovik, High-temperature surface superconductivity in topological flat-band systems, *Phys. Rev. B* **83**, 220503 (2011).
- [47] J. P. Perdew, K. Burke, and M. Ernzerhof, Generalized Gradient Approximation Made Simple, *Phys. Rev. Lett.* **77**, 3865 (1996).
- [48] N. Karnezos, L. B. Welsh, and M. W. Shafer, Structural and NMR properties of niobium dichalcogenides intercalated with post transition metals, *Phys. Rev. B* **11**, 1808 (1975).
- [49] C. S. Sunandana, K. Chandrasekaran, G. Aravamudan, and G. V. Subbarao, Electrical properties of InxMCh₂ (M ≡ Nb, Ta; Ch ≡ S, Se), *J. Less Common Metals* **84**, 115 (1982).
- [50] E. A. Marseglia, Transition metal dichalcogenides and their intercalates, *Int. Rev. Phys. Chem.* **3**, 177 (1983).
- [51] S. Grimme, J. Antony, S. Ehrlich, and S. Krieg, A consistent and accurate ab initio parametrization of density functional dispersion correction (DFT-D) for the 94 elements H-Pu, *J. Chem. Phys.* **132**, 154104 (2010); S. Grimme, S. Ehrlich, and L. Goerigk, Effect of the damping function in dispersion corrected density functional theory, *J. Comput. Chem.* **32**, 1456 (2011).
- [52] The experimental lattice parameters for InNbS₂ are $a = b = 3.34 \text{ \AA}$ and $c = 8.16 \text{ \AA}$. The coordinates of S are (1/3, 2/3, 0.32). The experimental lattice constants for InNbSe₂ are $a = b = 3.45 \text{ \AA}$ and $c = 9.27 \text{ \AA}$. The coordinates of Se are (0, 0,

- 0.31). The theoretical lattice constant for InNbS_2 are $a = b = 3.346 \text{ \AA}$ and $c = 8.11 \text{ \AA}$. The relaxed coordinates of S are $(1/3, 2/3, 0.306)$. The theoretical lattice constants for InNbSe_2 are $a = b = 3.41 \text{ \AA}$ and $c = 9.18 \text{ \AA}$. The relaxed coordinates of Se are $(0, 0, 0.316)$.
- [53] S. Y. Savrasov, Linear-response theory and lattice dynamics: A muffin-tin-orbital approach, *Phys. Rev. B* **54**, 16470 (1996).
- [54] P. Blaha, K. Schwarz, G. K. H. Madsen, D. Kvasnicka, and J. Luitz, *WIEN2K, An Augmented Plane Wave + Local Orbitals Program for Calculating Crystal Properties* (Technische Universität Wien, Vienna, 2001).
- [55] F. Tran and P. Blaha, Accurate Band Gaps of Semiconductors and Insulators with a Semilocal Exchange-Correlation Potential, *Phys. Rev. Lett.* **102**, 226401 (2009).
- [56] T. Fukui, Y. Hatsugai, and H. Suzuki, Chern Numbers in Discretized Brillouin Zone: Efficient Method of Computing (Spin) Hall Conductances, *J. Phys. Soc. Jpn.* **74**, 1674 (2005).
- [57] M. Taillefumier, V. K. Dugaev, B. Canals, C. Lacroix, and P. Bruno, Chiral two-dimensional electron gas in a periodic magnetic field: Persistent current and quantized anomalous Hall effect, *Phys. Rev. B* **78**, 155330 (2008).
- [58] In fact, both the LMTO and linearized augmented plane-wave methods assume improved projectors that include both the radial wave functions and their energy derivatives in order to better describe the orbital partial characters of the one-electron states. See O. K. Andersen, Linear methods in band theory, *Phys. Rev. B* **12**, 3060 (1975).
- [59] G. Resta, S.-T. Pi, X. Wan, and S. Y. Savrasov, High Surface Conductivity of Fermi Arc Electrons in Weyl semimetals, [arXiv:1708.02415](https://arxiv.org/abs/1708.02415).
- [60] For a review, see, e.g., F. Yonezawa and K. Morigaki, Coherent potential approximation: Basic concepts and applications, *Prog. Theor. Phys. Suppl.* **53**, 1 (1973).